

First-principles analysis of phonon thermal transport properties of two-dimensional WS_2/WSe_2 heterostructures

Zheng Chang(常征), Kunpeng Yuan(苑昆鹏), Zhehao Sun(孙哲浩), Xiaoliang Zhang(张晓亮), Yufei Gao(高宇飞), Xiaojing Gong(弓晓晶), and Dawei Tang(唐大伟)

Citation: Chin. Phys. B, 2021, 30 (**3**): 034401. DOI: 10.1088/1674-1056/abd2a6
Journal homepage: http://cpb.iphy.ac.cn; http://iopscience.iop.org/cpb

What follows is a list of articles you may be interested in

A phononic rectifier based on carbon schwarzite host-guest system

Zhongwei Zhang(张忠卫), Yulou Ouyang(欧阳宇楼), Jie Chen(陈杰), and Sebastian Volz
Chin. Phys. B, 2020, 29 (**12**): 124402. DOI: 10.1088/1674-1056/abbbf9

Scaling behavior of thermal conductivity in single-crystalline α-Fe_2O_3 nanowires

Qilang Wang(王啟浪), Yunyu Chen(陈允玉), Adili Aiyiti(阿地力·艾依提), Minrui Zheng(郑敏锐), Nianbei Li(李念北), Xiangfan Xu(徐象繁)
Chin. Phys. B, 2020, 29 (**8**): 084402. DOI: 10.1088/1674-1056/ab90f0

General theories and features of interfacial thermal transport

Hangbo Zhou(周杭波), Gang Zhang(张刚)
Chin. Phys. B, 2018, 27 (**3**): 034401. DOI: 10.1088/1674-1056/27/3/034401

SPECIAL TOPIC — Phononics and phonon engineering

First-principles analysis of phonon thermal transport properties of two-dimensional WS_2/WSe_2 heterostructures*

Zheng Chang(常征)[1], Kunpeng Yuan(苑昆鹏)[1], Zhehao Sun(孙哲浩)[1], Xiaoliang Zhang(张晓亮)[1,†], Yufei Gao(高宇飞)[1,‡], Xiaojing Gong(弓晓晶)[2,§], and Dawei Tang(唐大伟)[1,¶]

[1] *Key Laboratory of Ocean Energy Utilization and Energy Conservation of Ministry of Education, School of Energy and Power Engineering, Dalian University of Technology, Dalian* 116024, *China*

[2] *Institute of Materials Science and Engineering, National Experimental Demonstration Center for Materials Science and Engineering, Changzhou University, Changzhou* 213164, *China*

(Received 3 August 2020; revised manuscript received 7 December 2020; accepted manuscript online 11 December 2020)

The van der Waals (vdW) heterostructures of bilayer transition metal dichalcogenide obtained by vertically stacking have drawn increasing attention for their enormous potential applications in semiconductors and insulators. Here, by using the first-principles calculations and the phonon Boltzmann transport equation (BTE), we studied the phonon transport properties of WS_2/WSe_2 bilayer heterostructures (WS_2/WSe_2-BHs). The lattice thermal conductivity of the ideal WS_2/WSe_2-BHs crystals at room temperature (RT) was 62.98 W/mK, which was clearly lower than the average lattice thermal conductivity of WS_2 and WSe_2 single layers. Another interesting finding is that the optical branches below 4.73 THz and acoustic branches have powerful coupling, mainly dominating the lattice thermal conductivity. Further, we also noticed that the phonon mean free path (MFP) of the WS_2/WSe_2-BHs (233 nm) was remarkably attenuated by the free-standing monolayer WS_2 (526 nm) and WSe_2 (1720 nm), leading to a small significant size effect of the WS_2/WSe_2-BHs. Our results systematically demonstrate the low optical and acoustic phonon modes-dominated phonon thermal transport in heterostructures and give a few important guidelines for the synthesis of van der Waals heterostructures with excellent phonon transport properties.

Keywords: WS_2/WSe_2 bilayer heterostructures, thermal transport, first-principles, Boltzmann transport equation

PACS: 44.10.+I, 63.22.−m, 65.80.−g, 71.15.Mb **DOI:** 10.1088/1674-1056/abd2a6

1. Introduction

Transition metal dichalcogenides (TMDCs) have rapidly emerged and attracted tremendous interests in the microelectronic industry due to their innovative physical properties and many applications in devices. Their composition is usually expressed as MX_2 (M, transition metal element and X, chalcogen element), which can exist stably as monolayer, bilayer, and bulk crystal structures. Different from graphene, two-dimensional (2D) TMDCs materials, which have wide band gap and high electron mobility, can be seen as excellent candidates for semiconductor and optoelectronic devices.[1–4] Each transition metal atom layer in the 2D TMDCs material is sandwiched between two chalcogen atom layers, and their stability of in-plane direction is maintained by the covalent bonds. In contrast, the van der Waals interaction in the out-of-plane direction is relatively weak which can be sufficient for individual 2D crystals to keep free-standing.[1,5] Nowadays, a variety of 2D TMDCs materials, such as single-layer WS_2, WSe_2, etc., have been produced by chemical vapor deposition method[6,7] and extensive attempts have shown that the 2D TMDCs can be seen as one of the most promising thermoelectric materials at relatively high temperatures.[8,9]

Most recently, various thermoelectric materials have been designed for converting waste heat to electricity (Seebeck effect). The figure of merit (ZT) is used to evaluate the performance of thermoelectric materials based on $ZT = S^2\sigma T/\kappa$, which refers to the Seebeck coefficient (S), electrical conductivity (σ), and thermal conductivity (κ). The total thermal conductivity (κ) consists of electronic thermal conductivity (κ_{el}) and lattice thermal conductivity (κ_{lat}). Combining with the equation of ZT, it can be noticed that high S, high σ, and low κ are preferred to improve ZT.[10] Furthermore, anisotropic single-layer crystals[11] are also supposed to have high ZT[12] comparing with bulk crystals. Nevertheless, the occurrence is not noticeable in the 2D WX_2 (X = S, Se) crystals.[13] Heterostructures (e.g., WS_2/WSe_2-

*Project supported by the National Natural Science Foundation of China (Grant Nos. 51720105007, 51806031, 11602149, and GZ1257) and the Fundamental Research Funds for the Central Universities, China (Grant Nos. DUT16RC(3)116 and DUT19RC(3)006). The computing resources from Supercomputer Center of Dalian University of Technology and ScGrid are greatly acknowledged.

†Corresponding author. E-mail: zhangxiaoliang@dlut.edu.cn

‡Corresponding author. E-mail: gaoyufei@dlut.edu.cn

§Corresponding author. E-mail: gongxiaojing2018@cczu.edu.cn

¶Corresponding author. E-mail: dwtang@dlut.edu.cn

© 2021 Chinese Physical Society and IOP Publishing Ltd

BHs, MoS_2/$MoSe_2$-BHs) have attracted significant interest for their smaller band gap than those of single-layer MoS_2 and $MoSe_2$,[14] especially in the energy storage fields.[15–18]

It has been reported that the WS_2/WSe_2-BHs has concentrated on the arrangement of the density of states around the Fermi level and band gap.[19] The WS_2/WSe_2-BHs shows a reduced band gap compared to those of 2D WS_2 and WSe_2. It is generally accepted that alteration of the electronic band structure could be ascribed to the change of the weak vdW interaction.[14] In addition, for 2D WX_2 (X = S, Se) crystals, constructing heterostructure is an effective approach to enhance ZT because combining single-layer nanocrystals is an effective way to increase phonon anharmonicity.[20] Generally, a high ZT value is required by high performance thermoelectric materials and the reduction of κ_{lat} is also necessary.[21–23] Despite the electronics of the WS_2/WSe_2-BHs have been reported in recent years,[14] there is little quantitative analysis of their phonon transport properties until now.

The purpose of this paper is to investigate the phonon transport in the WS_2/WSe_2-BHs and theoretically explore alteration of phonon transport properties, which is attributed to the interlayer vdW interaction, by using first-principles calculations based on the density functional theory (DFT) together with an iterative solution of the phonon Boltzmann transport equation (BTE). In order to further reveal the difference of phonon transport mechanisms between the WS_2/WSe_2-BHs and single-layer WS_2 and WSe_2, we also calculated and studied the charge transfer across the interface and representative phonon mean free paths (MFPs) of the WS_2/WSe_2-BHs.

2. Model system and computational methodology

2D TMDCs emerge 2H phase (hexagonal symmetry) with the MX_2, where M represents W or Mo; X represents Te, Se, or S. The WS_2/WSe_2-BHs, including a single (S/Se)-W-(S/Se) layer with space group $P\bar{6}M2$ (No. 187), which has no inversion symmetry and is shown in Fig. 1. On the vertical direction of the WS_2/WSe_2-BHs, the Se and W atoms at the bottom are completely overlayed by the W and S atoms at the top, respectively. The optimized lattice parameters of the WS_2/WSe_2-BHs formed as hexagonal structure are $a = b = 3.53$ Å, and interlayer distance $d = 3.53$ Å ties well with previous theoretical calculations.[14,24] Considering the lattice mismatch can lead to stack disorder or Moiré pattern superstructures, we also calculated its intrinsic lattice mismatch δ ($\delta < \pm 5\%$) with $\delta = 100\% \times (a_1 - a_2)/a_2$, where a_1 and a_2 are the lattice parameters of 2D WS_2 and WSe_2, respectively. The calculated value of $\delta = -3.7\%$ is in good agreement with previous studies,[24,25] and proves the stability of the WS_2/WSe_2-BHs.

The crystal structure of WS_2/WSe_2-BHs has been optimized by first-principles calculations within the framework of DFT, as employed in the Vienna *ab-initio* simulation package (VASP).[26] The Perdew–Burke–Ernzerhof (PBE) functional with generalized gradient approximation (GGA)[27] is adopted to describe the electron exchange and correlation functional. The planewave cutoff energy and k-point sampling are set to be 550 eV and $11 \times 11 \times 1$ grid within Monkhorst–Pack[28] scheme, respectively, and the energy convergence threshold is set as 10^{-6} eV. The effect of vdW interaction is considered in all simulations with dispersion corrected DFT method (vdW-DF-revPBE),[29] which has been proven reliable for the vertically stacked system.[30] Moreover, we imposed a vacuum spacing larger than 20 Å to avoid the interactions among heterostructures neighboring layers in the periodic slabs. All atoms in the crystals system are fully relaxed until Hellmann-Feynman force on each ion is less than 10^{-4} eV·Å^{-1}.

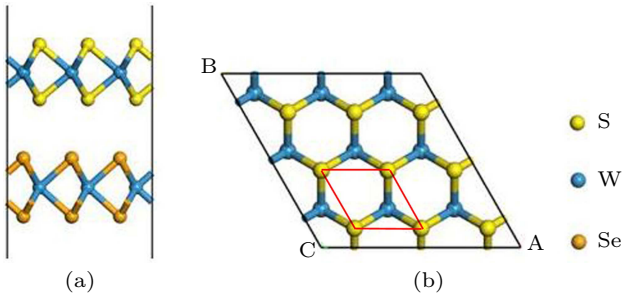


Fig. 1. Optimized crystals structure of the WS_2/WSe_2-BHs. (a) Local side view and (b) top view.

The k_{lat} of a material can be computed by solving the linearized BTE for phonons, as employed in the ShengBTE code.[31,32] It can be expressed as

$$\kappa_{\mathrm{lat},\alpha\beta} = \sum_{q,s} C_v(qs)\, v^{\alpha}(qs)\, v^{\beta}(qs)\, \tau_{qs}, \tag{1}$$

where $v^{\alpha}(qs)$ represents the phonon group velocity along the α-th direction, τ_{qs} represents the phonon lifetime, q and s denote the wave vector and branch index of specific phonon mode, respectively. $C_v(qs)$ refers to the heat capacity at constant volume for each phonon mode, and it can be written as

$$C_v(qs) = \frac{k_{\mathrm{B}}}{NV} \frac{(\hbar\omega/k_{\mathrm{B}}T)^2\, e^{\hbar\omega/k_{\mathrm{B}}T}}{\left(e^{\hbar\omega/k_{\mathrm{B}}T} - 1\right)^2}, \tag{2}$$

where k_{B} and N represent the Boltzmann constant and the total number of q-points in the Brillouin zone (BZ). T and $\hbar$ represent the absolute temperature and the reduced Planck constant, respectively. ω and V represent the phonon angular frequency and the volume of unit cell.

We first calculated the phonon dispersion of the WS_2/WSe_2-BHs and used $3 \times 3 \times 1$ supercell containing 54 atoms. The Γ point mesh of $1 \times 1 \times 1$ is applied to sample the BZ. The density functional perturbation theory (DFPT) as applied in the VASP code[26] is used to compute harmonic second-order interatomic force constants (IFCs). Then, the phonon dispersion within the frozen phonon approximation and phonon density of states (PhDOS) are also computed

by using the PHONOPY code.[33] Considering the existence of long-range electrostatic interactions of the polar materials, non-analytical terms are added to the dynamical matrices, and the corresponding parameters, including Born effective charge tensor and the dielectric tensor, are obtained from DFPT. With the aim to get the precise value of $\kappa_{\rm lat}$, anharmonic third-order IFCs are also taken into account. Specifically speaking, the $3\times3\times1$ supercell and $1\times1\times1$ Γ point mesh for calculating anharmonic third-order IFCs are used in the script of the thirdorder.py.[31] For the $\kappa_{\rm lat}$ calculations, the $90\times90\times1$ of q-grid is used, and it should be well converged for the calculation of $\kappa_{\rm lat}$.

First-principles-based predictions of $\kappa_{\rm lat}$ from perturbation theory have attained significant achievement only considering three-phonon scattering. Furthermore, four-phonon and higher-order processes are multi-phonon processes, and their evaluations have been a long standing and significant challenge for decades.[34] Recently, more and more theoretical results have proved that the effect of four-phonon and higher-order phonon scattering processes are very little in most semiconductors.[35–37] Thus, only three-phonon scattering processes are considered in this paper, and the role of four-phonon and higher-order scattering processes have been ignored.

3. Results and discussion

3.1. Phonon dispersion

For vertically stacking 2D WS_2 on top of 2D WSe_2, the newly formed WS_2/WSe_2-BHs still holds the 2H phase. Since phonon dispersion curves are crucial for the calculation of phonon transport, the phonon dispersion curves of the WS_2/WSe_2-BHs along some high symmetry lines and PhDOS are plotted in Fig. 2. The WS_2/WSe_2-BHs unit cell has six atoms resulting in eighteen phonon branches. As shown in Fig. 2, one notable information in the phonon dispersion curves is a small gap between the lowest optical mode and the highest acoustic mode. Since vdW forces hold WX_2 (S, Se) single-layers together in the WS_2/WSe_2-BHs, the vdW force assists in stabilizing the WS_2/WSe_2-BHs and eliminating the imaginary phonon modes. The $k*$ theorem theory[38–40] for phonons is applied with sorting the phonon modes of the WS_2/WSe_2-BHs under the continuousness of their eigenvectors, and it can be expressed as

$$\left|\sum e^{*}_{\kappa,\sigma_1}(j)\cdot e_{\kappa+\Delta,\sigma_2}(j)\right| = \left|\delta_{\sigma_1,\sigma_2} - o(\Delta)\right|, \tag{3}$$

where $e^{*}_{\kappa,\sigma_1}(j)$ represents the displacement of the atom j in the eigenvector of (k,σ) vibrational mode and Δ represents a small wave vector.

In crystals, the potential energy Φ is assumed to be an analytic function of the displacement (r) of the atoms.[41] When the fully optimized crystal structure is stable, its potential energy continuously increases against any mixtures of atomic displacements. Specifically, a mechanically stable crystal needs to obey the equilibrium, $\partial\Phi/\partial r=0$. The phonon modes with their color weighted for the contribution of W, Se, and S atoms have been calculated to ensure that the fully relaxed crystal of the WS_2/WSe_2-BHs is located at a minimum on the potential energy surface. All the phonon modes together with their widths are weighted in the qualitative representation characteristics of vibration modes including the contribution of atoms and their direction and amplitude, named fat bands.

The fat bands for W(xy), W(z), Se (S)(xy), and Se (S)(z) vibrations are displayed in Figs. 2(a)–2(c), and the corresponding PhDOS of the WS_2/WSe_2-BHs is shown in Fig. 2(d). The absence of phonon modes with negative frequencies indicates that the WS_2/WSe_2-BHs is dynamically stable at 0 K. It also worth to mention that there are hybridizations among the W(xy) and W(z) vibrations for quite a few phonon modes, while these optical modes above 10 THz almost express no vibrations in Fig. 2(a). The non-orthogonality of the covalent W–Se and W–S bonds can result in the W(xy-z) hybridization. Moreover, it is crucial to highlight that the Se(z) vibration occupies the main percentage closing to within the Γ point signified by the black circles in Fig. 2(b). This hybridization is consistent with the consequence of 2D WS_2, which is caused by the singular interlayer crystal symmetry.[39,42] The layer of W atom is sandwiched between two S (Se) layers for the WS_2/WSe_2-BHs, which makes the xy direction and z direction vibrations of the W atom layers be independent from each other. Further, combining with the projected PhDOS plotted in Fig. 2(d), it is worthwhile mentioning that the W atoms are to be occupied by important parts at all the different phonon modes. However, the Se (S) atoms play a dominant role in medium low frequency (5–8 THz) and high frequency (8–12 THz) areas, respectively. More interestingly, there are several peaks in the optical phonon modes region, which indicates the smaller phonon group velocity.

Both harmonicity and anharmonicity of phonon show close relationship with the $k_{\rm lat}$. The phonon group velocity is an important parameter to describe the phonon harmonicity. To fundamentally understand the mechanisms of the $k_{\rm lat}$ changed from 2D WS_2, the WS_2/WSe_2-BHs to 2D WSe_2, the phonon dispersion curves of the above models are calculated. The calculated phonon dispersion curves of 2D WS_2, 2D WSe_2, and WS_2/WSe_2-BHs are plotted in Figs. 3(a)–3(c). From these figures, we also observe that both 2D WS_2 and WSe_2 have three acoustic modes, i.e., two linear acoustic modes [one transverse (TA_1), one longitudinal (LA_1)] and one quadratic flexural acoustic branch (ZA_1). The TA_1 and LA_1 display linear dependences closing to the Γ point, which is accordance with the previous works.[43,44] As the symmetry in the crystal

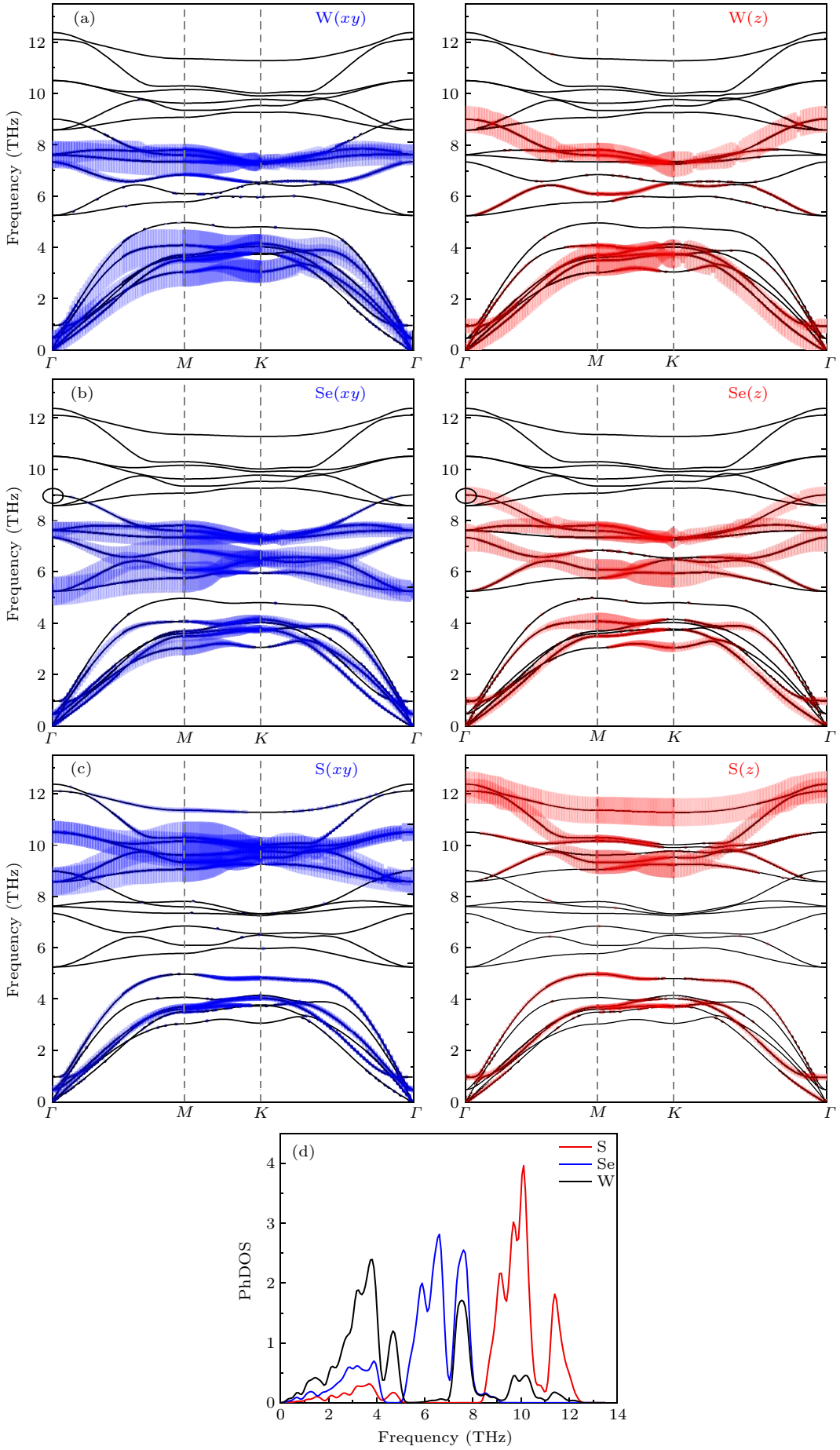


Fig. 2. (a)–(c) Phonon dispersion curves with fat bands indicating movements of atomic vibrations and (d) PhDOS of the WS_2/WSe_2-BHs.

structure is the same, there is great similarity for phonon dispersion curves of the 2D WS_2 and WSe_2 except for comparatively higher phonon frequencies of 2D WS_2. The reason is that the mass of Se (78.96 amu, 1 amu $= 1.660539 \times 10^{-27}$ kg) is much heavier than that of S (32.065 amu). Meanwhile, the average Debye temperature (TD) is defined by[45]

$$\frac{1}{\theta_{\mathrm{D}}^3} = \frac{1}{3}\left(\frac{1}{\theta_{\mathrm{LA}}^3} + \frac{1}{\theta_{\mathrm{TA}}^3} + \frac{1}{\theta_{\mathrm{ZA}}^3}\right), \tag{4}$$

where θ_i is the acoustic mode ($i = \mathrm{LA}, \mathrm{TA}, \mathrm{ZA}$) and it has been obtained by $\theta_i = \hbar\omega_{i,\max}/k_{\mathrm{B}}$. $\omega_{i,\max}$ represents the largest acoustic frequency of the i-th acoustic mode. The average Debye temperature of 2D WSe_2 has been computed to be 158.85 K, which is lower than those of the WS_2/WSe_2-BHs (225.55 K) and 2D WS_2 (245.7 K). It can be found that the θ_i in 2D WSe_2 is significantly lower than that in the WS_2/WSe_2-BHs and 2D WS_2.

As for the WS_2/WSe_2-BHs, it has another three low frequency optical modes, defined as ZA_2, TA_2, and LA_2. In Fig. 3(c), it can be also observed that the LA_1 and ZA_2 intersect with each other, which results in the changing shape of LA_1. Closing to the kinks, the LA_1 branch becomes softened, which means the reduction of phonon group velocity. These phenomena have also been found in the other bilayer structures, which can be seen as the effects of the weak vdW interaction.[10,46,47]

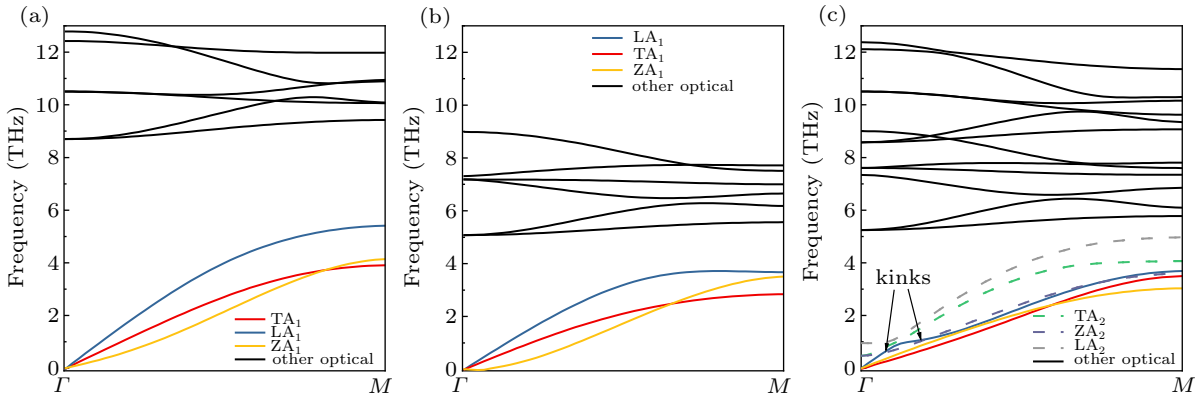


Fig. 3. Phonon dispersion curves of the acoustic and relatively low-lying optical phonon modes alongside the high symmetric path Γ–M in the BZ for (a) 2D WS_2, (b) 2D WSe_2, and (c) WS_2/WSe_2-BHs.

3.2. Lattice thermal conductivity

Recently, the previous review has illustrated that the cutoff of anharmonic interaction is the key to the computation of the κ_{lat}.[48] While too large cutoff radius usually leads to much more computational resources, a small cutoff may overestimate the value of κ_{lat}. Therefore, the convergence of the κ_{lat} with regard to the cutoff radius of anharmonic IFCs should be investigated firstly. Qin and Hu recently proposed that[49] based upon the analysis of harmonic IFCs, the cutoff radius can be directly determined to gain the acceptable value of κ_{lat}. To better understand the strength of the interatomic interactions, the normalized trace of IFC tensors needs to be computed.[50] According to this parameter, we can directly determine how large the cutoff radius would be to quantitatively assess the anharmonic IFCs by the meaning of containing the strength of this probably strong interactions as exposed by the large trace value. It can be clearly seen in Fig. 4(a) that the reasonable cutoff is a distance of 0.72 nm, and over 9$^{\mathrm{th}}$ nearest neighbors have extremely weak trace values, representing negligible anharmonic IFCs. As proved for the convergence investigation of the κ_{lat} in Fig. 4(b), there is a striking drop for the κ_{lat} to the rear of taking account for the 3$^{\mathrm{th}}$ nearest neighbors and the computed κ_{lat} meets rapidly up to the 9$^{\mathrm{th}}$ nearest neighbors. This is consistent with the observation and evaluation from the strength of the harmonic IFCs in Fig. 4(a). Guo *et al.* calculated the value of κ_{lat} of the $MoSe_2/WS_2$-BHs taking an interaction range of 0.63 nm

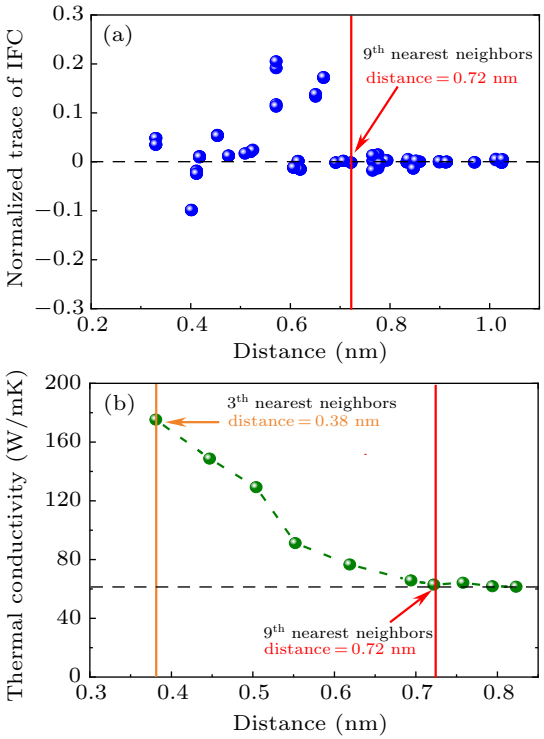


Fig. 4. (a) Normalized traces of IFC tensors versus atomic distances and (b) convergence examination of the κ_{lat} with regard to the cutoff radius.

for the anharmonic IFCs.[51] Hence, taking into account of computational price and accuracy, the interactions up to the 9th nearest neighbors are considered for the anharmonic IFCs computations.

Based on the converge test of anharmonic IFCs, we plot the computed κ_{lat} of 2D WS_2, WSe_2, and the WS_2/WSe_2-BHs as a function of temperature ranging from 200 K to 1000 K in Fig. 5(a), the κ_{lat} of these three systems decrease continuously with increasing temperature. In Table 1, we have listed the computed values of κ_{lat} for 2D WS_2 and WSe_2 together with the WS_2/WSe_2-BHs at RT. For 2D WSe_2, the lattice thermal conductivity, about 46.8 W/mK, is close to one half of that of 2D WS_2. For comparison, some results of previous studies are also shown in Table 1.[8,42,44,52–54] It should be pointed out that our calculated results for the 2D crystals are in accordance with the previous theoretical calculations[54] and experimental measured[53] data. Our calculated lattice thermal conductivities of 2D crystals are a little higher than the experimental measured values due to the lack of impurity, defect, and edge as scatters in our model. Combining our calculation, we obtain κ_{lat} of 62.98 W/mK for WS_2/WSe_2-BHs at RT, which is between those of single-layer WS_2 and WSe_2. Furthermore, it is slightly lower than the average κ_{lat} value (74.27 W/mK) of single-layer WS_2 and WSe_2.

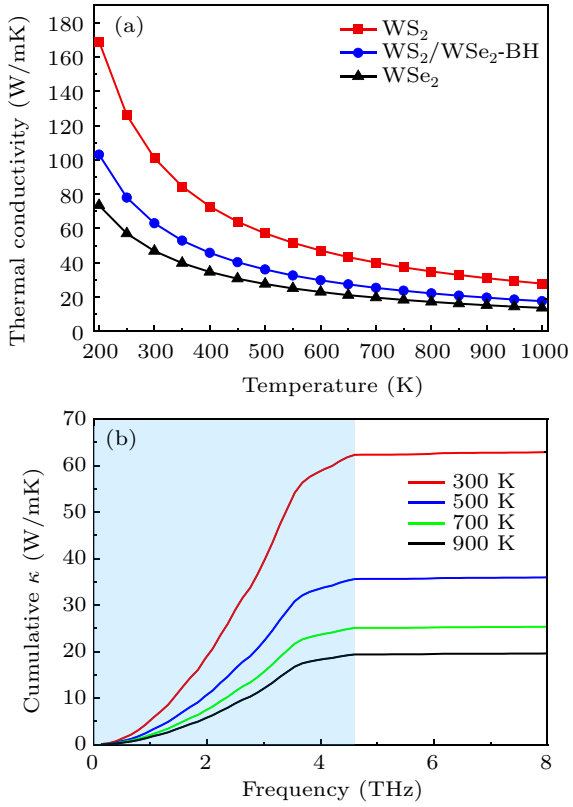


Fig. 5. (a) The computed κ_{lat} versus temperature for WS_2/WSe_2-BHs, 2D WS_2, and 2D WSe_2. (b) The cumulative κ versus the frequency for WS_2/WSe_2-BHs. The low frequency range (< 4.73 THz) is scratched in blue.

In order to deeply explore and understand the major heat carriers of the WS_2/WSe_2-BHs, we have calculated the normalized cumulative lattice thermal conductivity κ as a function of phonon frequency at 300 K, 500 K, 700 K, and 900 K, as shown in Fig. 5(b). It can be noticed that the phonon branches with a frequency lower than 4.73 THz contribute nearly 90% to the κ_{lat}, which indicates that the three acoustic branches and some low lying optical branches play a dominant role in the heat transport of the WS_2/WSe_2-BHs.

Table 1. Calculated in-plane κ_{lat} of 2D WS_2 and WSe_2 along with the WS_2/WSe_2-BHs at RT.

Materials	Methods	κ_{lat} (W/mK)
2D WS_2	Expt.	32,[52] 120[53]
	DFT	142,[42] 125 ± 25,[54] 31.8[44]
	this work	101.74
2D WSe_2	Expt.	42[53]
	DFT	42,[8] 50 ± 5,[54] 53[42]
	this work	46.8
WS_2/WSe_2-BHs	this work	62.98

Some previous work reported κ_{lat} of 2D materials with sample length around 10 μm long or sufficiently large spans about three orders of magnitude.[42,55,56] We have calculated the κ_{lat} of the WS_2/WSe_2-BHs, 2D WS_2, and WSe_2 as a function of temperature for several sample lengths and infinite length for comparison, as shown in Fig. 6. It can be noticed that the κ_{lat} decreases with decreasing sample lengths of the studied model structures because of increased phonon–boundary scattering. For the cases of the length being 10 μm, 1 μm, and 0.1 μm, the 300 K lattice thermal conductivity of the WS_2/WSe_2-BHs, compared with that of the infinite case, is reduced by about 2.6%, 20.7%, and 69.2%, respectively. The results of the single-layer materials are entirely lower than the corresponding values of 30.9%, 56.6%, and 82.4% for WSe_2, 5.6%, 35.5%, and 82.6%, respectively.

There is no denying that generally classical phonon size effects, which are employed to understand phonon MFPs with the characteristics length, were being significantly discovered in the microscale and nanoscale system.[57] If the size of the device refers to as small as the phonon MFP, the cumulative κ should considerably reduce due to the frequent phonon–surface scattering. Therefore, the knowledge of MFP holds indispensable to focus on the size effects and is another key to understanding the phonon transport properties of nanocrystals, we also match the result to a single parametric function[31]

$$\kappa(l \leq l_{max}) = \frac{\kappa_0}{1 + l_0/l_{max}}, \tag{5}$$

where κ_0 and l_{max} represent the ultimate cumulative lattice thermal conductivity and the maximum MFP involved. l_0 is an assessment parameter to compute.

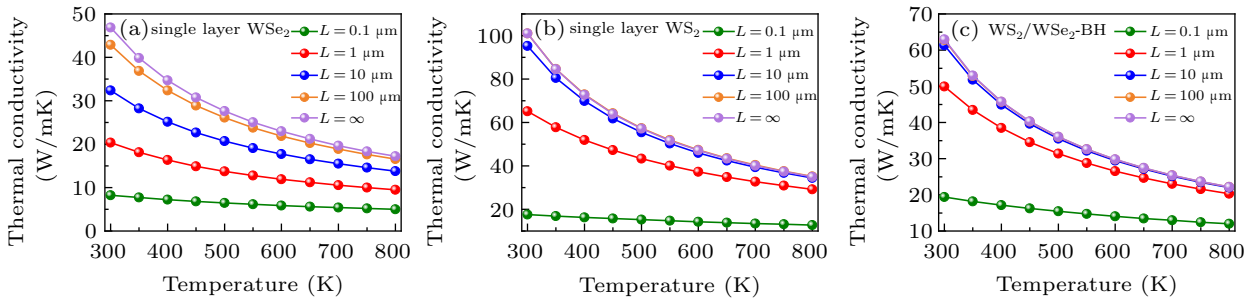


Fig. 6. The lattice thermal conductivity variation of single-layer WSe_2 (a), WS_2 (b), and the WS_2/WSe_2-BHs (c) as function of temperature for different sample lengths (here infinite length sample, $L = \infty$, refers to the case without phonon–boundary scattering).

These matched phonon dispersion curves included as mapped with dot lines in Fig. 7, reproduce together the slope and the location of the computed result reasonably well. The cumulative κ of the WS_2/WSe_2-BHs, 2D WS_2, and WSe_2 keep increasing as MFP increases, up to until reaching the thermodynamic limit. It yields the parameter l_0 of 233 nm, 526 nm, and 1720 nm that can analyze and understand the illustrative MFP of the WS_2/WSe_2-BHs, 2D WS_2, and WSe_2, respectively. Compared to the l_0 of 526 nm and 1720 nm for 2D WS_2 and WSe_2, the WS_2/WSe_2-BHs shows fundamentally smaller l_0 values. As a result, the size dependence of the value of κ for the WS_2/WSe_2-BHs is not so significant. Meanwhile, the phonon MFPs which contribute most to the total κ of the WS_2/WSe_2-BHs, 2D WS_2, and 2D WSe_2 are in the ranges of 60–600 nm, 100–2000 nm, and 100–40000 nm, respectively.

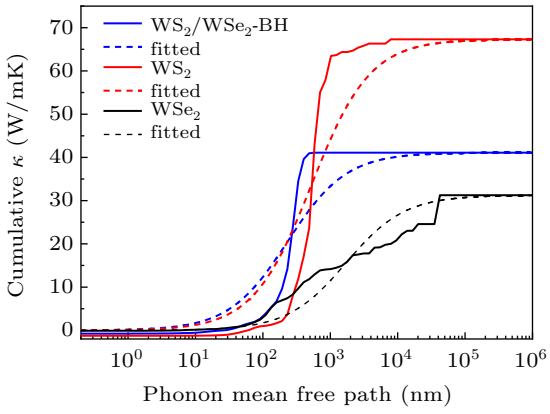


Fig. 7. Cumulative κ of the WS_2/WSe_2-BHs, 2D WS_2, and 2D WSe_2 versus the maximum phonon MFP at RT. The dot lines are drawn with curves, matching the above single parametric function.

3.3. Phonon group velocities and lifetimes

To analyze the thermal transport mechanism of heterostructure, the phonon group velocities and phonon lifetimes of the three models and different phonon branches in the heterostructure are compared in Fig. 8. Phonon group velocities can be obtained directly by the slope of the phonon modes. Below, we have computed the group velocities of the phonon modes ω_s by the slope of the phonon modes, which can be given by[58,59]

$$\nu(qs) = \frac{\partial \omega_s(q)}{\partial q}. \tag{6}$$

On the other side, we also calculated the phonon lifetimes by the phonon linewidth $2\Gamma_{qs}(\omega)$ of the phonon modes[58,60]

$$\tau_{qs} = \frac{1}{2\Gamma_{qs}(\omega)}, \tag{7}$$

where $\Gamma_{qs}(\omega)$ is a form analogous to the Fermi's golden rule and completely incorporates scatterings from the entire phonon modes.[61]

From Fig. 8(a), we can observe that most of the ν decrease with increasing frequency because of the unstiffened phonon modes. The ν of the acoustic and optical branches in the relatively low frequency region are those in the high frequency range. Thus, the low frequency acoustic and optical branches play a dominant role in phonon transport. More importantly, one interesting phenomenon is that the ν of the optical branches is even larger than those of acoustic branches which is rarely reported in the previous literature. Figure 8(b) displays that the frequency dependent group velocity of the WS_2/WSe_2-BHs is comparable with that of 2D WS_2 and WSe_2. From Fig. 8(b), it should be noted that the highest ν of the WS_2/WSe_2-BHs (5.18 km·s^{-1}) is comparatively higher than that of the 2D WS_2 (4.75 km·s^{-1}) and 2D WSe_2 (4.48 km·s^{-1}) at relatively low frequency region. To compare the group velocity completely, the average values of the WS_2/WSe_2-BHs, 2D WS_2, and WSe_2 are calculated and are 0.53 km·s^{-1}, 0.67 km·s^{-1}, and 0.52 km·s^{-1}, respectively. The phonon lifetimes considering all kinds of scattering processes, including boundary scattering, defect scattering, and phonon–phonon Umklapp scattering, are also compared in Fig. 8(c). In Fig. 8(c), it is worthwhile mentioning that the distributions of τ at low frequency acoustic and optical modes (lower than 4 THz) are frequency-independent. Figure 8(d) displays the frequency dependence of τ of the three models. It can be found that the τ of the WS_2/WSe_2-BHs are distributed between those of 2D WS_2 and WSe_2, especially in the relatively high frequency range (greater than 8 THz). The variation trend of the τ is consistent with the κ_{lat} of the WS_2/WSe_2-BHs, 2D WS_2, and WSe_2. Combining the results presented in Figs. 2, 3, and 8, we conclude that the vdW interfacial interaction leads to a change in the Debye temperature and weakens the group velocities of phonon branches of the WS_2/WSe_2-BHs. These results can result in the reduction of the κ_{lat} according to the Slack's theory.[62]

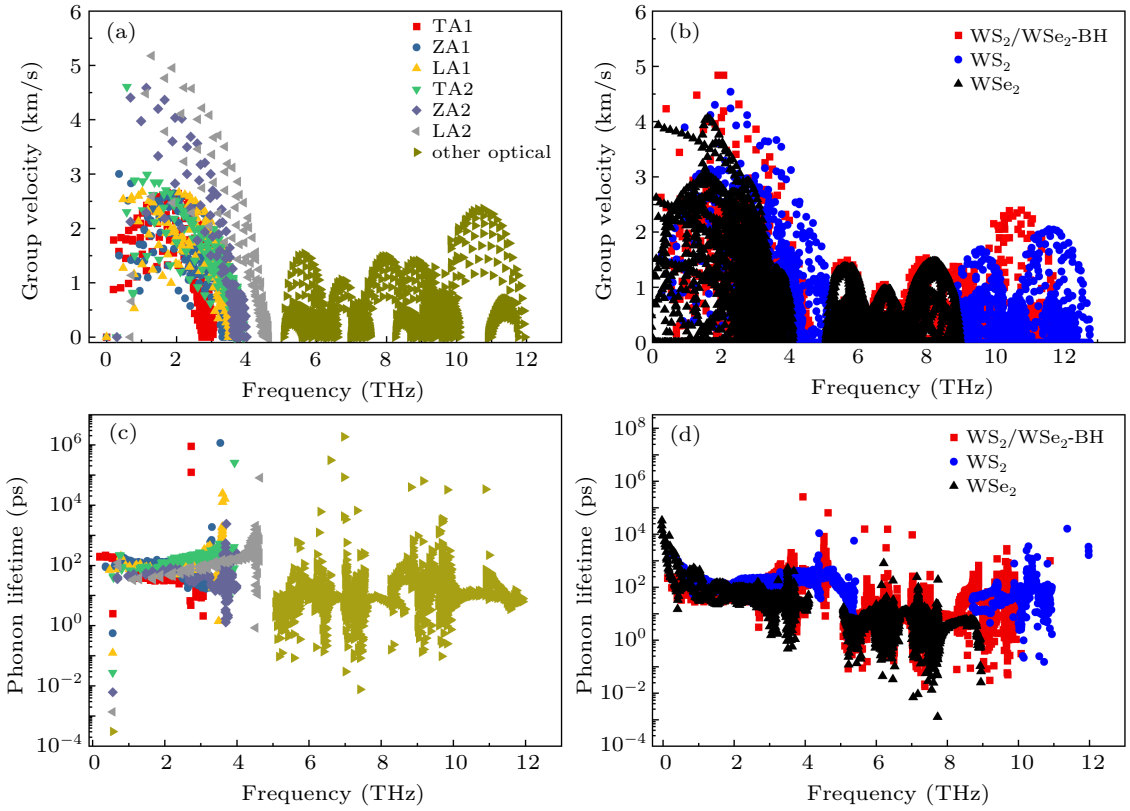


Fig. 8. Frequency versus (a) phonon group velocities (v) and (c) phonon lifetimes (τ) of the whole phonon branches at RT for WS_2/WSe_2-BHs. Frequency versus (b) v and (d) τ at RT for WS_2/WSe_2-BHs, 2D WS_2, and 2D WSe_2.

To further understand the intrinsic physical mechanism of phonon transport and clarify the differences between the three materials, we have calculated the three-phonon scattering process and the Grüneisen parameter. Aimed at the three-phonon scattering process, it is significant to understand how a multitude of scattering channels are available for phonons to be scattered. For further insight into the τ, the three-phonon scattering phase space (P_3), which can qualitatively describe the three-phonon scattering process including the N and U processes, is calculated using the following equation[61] and plotted in Fig. 9:

$$P_3 = \frac{2}{3\Omega}\left(P_3^{(+)} + \frac{1}{2}P_3^{(-)}\right), \tag{8}$$

$$P_3^{(\pm)} = \sum_j \int \mathrm{d}q D_j^{(\pm)}(q), \tag{9}$$

where Ω represents the normalization factor equivalent to the unlimited phase space for each scattering type and $D_j^{(\pm)}$ represents the absorption and emission processes. Comparing Figs. 8(d) and 9, we can see clearly that the changing trend of the P_3 of 2D WS_2 and WSe_2, which exists steadily with the finding in the whole τ, including a larger phonon gap. Such a large gap can hinder P_3 process because it is hard to satisfy the scattering rules, which results in a large τ. Based on the results above, the WS_2/WSe_2-BHs has a larger κ_{lat} compared with 2D WSe_2, while it expresses a larger P_3. To analyze this unexpected phenomenon, we have calculated the Grüneisen parameter, which determines the strength of each phonon mode channel.

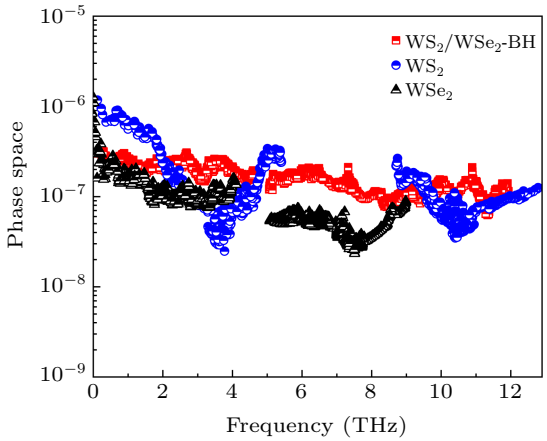


Fig. 9. Comparison of the P_3 phase space with respect to frequency for the WS_2/WSe_2-BHs, 2D WS_2, and WSe_2.

3.4. Grüneisen parameters

The Grüneisen parameter γ, which provides the anharmonicity information of models, is suitable to analyze and understand the thermal transport properties of nanomaterials. The expression of γ can be written as[63]

$$\gamma = \frac{3\alpha B V_{\mathrm{m}}}{C_V}, \tag{10}$$

where α represents the linear thermal expansion coefficient, V_{m} and B represent the molar volume and the bulk modulus, respectively, and C_V refers to the phonon volumetric specific

heat. The mode γ is described as[44]

$$\gamma_s(q) = -\frac{a_0}{\omega_s(q)}\frac{\partial \omega_s(q)}{\partial a}, \tag{11}$$

where $\omega_s(q)$ represents the frequency of the s-th phonon mode, and a_0 represents the equilibrium lattice parameter at 0 K.

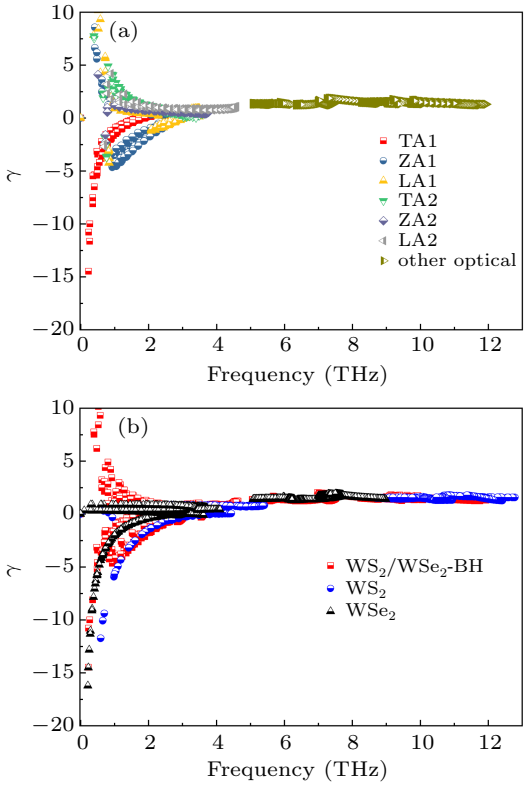


Fig. 10. (a) Calculated γ parameters versus the frequency of the whole phonon branches for WS_2/WSe_2-BHs. (b) Calculated γ parameters virus the frequency for WS_2/WSe_2-BHs, 2D WS_2, and WSe_2.

The calculated γ of WS_2/WSe_2-BHs are depicted in Fig. 10(a). The γ of ZA_1 located at the relatively low frequency region displays a large positive and fractional negative, which is consistent with 2D WS_2 and WSe_2.[64] It has previously been observed and focused on the other 2D structures such as graphene, and is mainly caused by the influence of membrane.[65] The large value of $|\gamma|$ for the phonon modes usually demonstrates strong anharmonicity which gives rise to the low value of k_{lat}. Obviously, the value of $|\gamma|$ of TA_1 reaches to 15 at the Γ point, indicating that the phonon mode expresses strong phonon–phonon anharmonicity. Furthermore, in Fig. 10(a), large $|\gamma|$ almost exists in the relatively low frequency region (< 4.73 THz), which significantly contributes to the anharmonic effect for the WS_2/WSe_2-BHs. Generally, for the materials, including lone-pair electrons, the non-bonded electrons influenced with the valence electrons of the neighboring atoms, would lead to increased anharmonicity at controlled temperature.[66] From Fig. 10(b), the γ of high frequency optical modes nearly keep as a constant, which indicates that the contribution of the optical modes to the anharmonic effect is very little. Moreover, we have also found that the WS_2/WSe_2-BHs possesses a smaller γ comparing with 2D WSe_2, which will lead to a larger κ_{lat} of the heterostructure.

3.5. Charge density distribution

As mentioned above, the atomic vibrations perpendicular to the xy plane are affected by the vdW interaction. For the modification on the elastic modulus of nanostructure resulted from the interface charges,[67] the interface effects usually play a significant role in exploring phonon and thermal transport properties of the vdW heterostructures. Therefore, the distribution of charge density difference of the WS_2/WSe_2-BHs and the charge redistribution and transfer among the single-layer WS_2 and WSe_2 surfaces can be gained as shown in Fig. 11. The charge density difference ($\Delta\rho$) can be obtained by

$$\Delta\rho = \rho_{(WS_2/WSe_2)} - \rho_{(WS_2)} - \rho_{(WSe_2)}, \tag{12}$$

where $\rho_{(WS_2/WSe_2)}$, $\rho_{(WS_2)}$, and $\rho_{(WSe_2)}$ correspond to the charge densities of WS_2/WSe_2-BHs, single-layer WS_2 and WSe_2, respectively. The average plane charge density difference $\Delta\rho(Z)^{avg}$ along the Z direction is described as

$$\Delta\rho^{avg}(Z) = \int \mathrm{d}x\mathrm{d}y\Delta\rho = \sum_{ij}\Delta x_i \Delta y_j \Delta\rho_{i,j}. \tag{13}$$

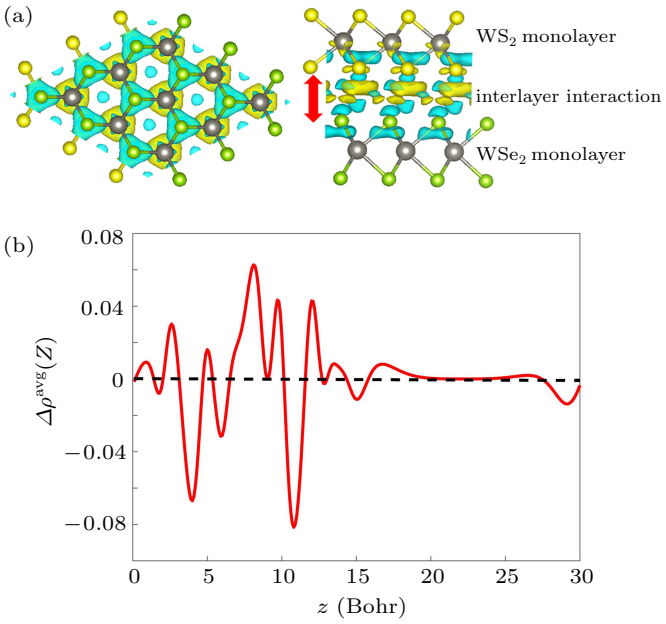


Fig. 11. (a) The top- and side-views of charge transfer across the interface of the WS_2/WSe_2-BHs. (b) The average plane charge density difference $\Delta\rho^{avg}(Z)$ along the Z direction for the WS_2/WSe_2-BHs. The gray, yellow, and green spheres indicate W, S, and Se atoms, respectively.

The data of the charge transfer (gaining and losing electron) among the atoms can be obtained from the charge density difference. In Fig. 11, we can notice that the charge decreases mostly at the Se atoms, in addition it increases at the S atoms, making electron–hole pairs dispersed for the WS_2/WSe_2-BHs interface. To estimate the charge transfer, the plane-averaged charge density difference $\Delta\rho(Z)^{avg}$ along the Z direction is

plotted in Fig. 11(b). There are many reasons for the charge transfer, having a weak orbital overlap among the heterostructures, the polarization and potential gradient fields of adjacent layers.[68] From Fig. 11(b), it can be noticed that the transferred interlayer charge density can reach to (~ 0.06 *e*/Bohr) due to the existence of vdW, which can significantly improve the anharmonic scattering among propagating phonons along the plane direction and consequently diminish the $\kappa_{\rm lat}$. It is well known that three factors, including the interfacial interaction, charge redistribution, and electron–hole pair separation, are generally supplemented by an improvement in optical transitions in the vdW heterostructures.[69] Based on the above analysis, we can understand the change of $\kappa_{\rm lat}$ of the WS_2/WSe_2-BHs from the perspective of charge transfer.

4. Conclusion

The phonon transport properties of the WS_2/WSe_2-BHs were systematically studied by the linearized phonon BTE combined with the conventional first principles method. We found that the $\kappa_{\rm lat}$ of the WS_2/WSe_2-BHs was about 62.98 W/mK at room temperature. The result demonstrates that the three-phonon scattering plays an important role in phonon transport, and that the three acoustic modes are the main heat carriers. We compared the average $\kappa_{\rm lat}$ value (74.27 W/mK) of WS_2 and WSe_2 single-layers with that of the WS_2/WSe_2-BHs, and found that the interlayer coupling and the kinks in acoustic branches result in the variation of the $\kappa_{\rm lat}$. Additionally, we obtained a parameter l_0 of 233 nm for the WS_2/WSe_2-BHs, and it is critical to thermal management with nanostructured crystals. Lattice thermal conductivity can be effectively modulated when the nanostructure scope is below the representative phonon MFP. The purpose of this work aims at understanding the mechanism of phonon transport in vertically stacking TMDCs heterostructures and further promoting their thermal management applications in optoelectronics and thermoelectric materials.

Data availability

The data that support the findings of this study are available from the corresponding author upon reasonable request.

References

[1] Jariwala D, Sangwan V K, Late D J, Johns J E, Dravid V P, Marks T J, Lauhon L J and Hersam M C 2013 *Appl. Phys. Lett.* **102** 173107
[2] Terrones H, López-Urías F and Terrones M 2013 *Scientific Reports* **3** 1
[3] Zhao W, Ribeiro R M, Toh M, Carvalho A, Kloc C, Castro Neto A and Eda G 2013 *Nano Lett.* **13** 5627
[4] Liu X and Zhang Y W 2018 *Chin. Phys. B* **27** 034402
[5] Mak K F, Shan J and Heinz T F 2011 *Phys. Rev. Lett.* **106** 046401
[6] Li H, Wu J, Yin Z and Zhang H 2014 *Accounts of Chemical Research* **47** 1067
[7] Tongay S, Fan W, Kang J, Park J, Koldemir U, Suh J, Narang D S, Liu K, Ji J and Li J 2014 *Nano Lett.* **14** 3185
[8] Kumar S and Schwingenschlögl U 2015 *Chemistry of Materials* **27** 1278
[9] Gandi A N and Schwingenschlögl U 2014 *Chemistry of Materials* **26** 6628
[10] Ma J J, Zheng J J, Zhu X L, Liu P F, Li W D and Wang B T 2019 *Phys. Chem. Chem. Phys.* **21** 10442
[11] Gao Y, Zhang X, Tang D and Hu M 2019 *Carbon* **143** 189
[12] Hicks L and Dresselhaus M S 1993 *Phys. Rev. B* **47** 12727
[13] Adessi C, Thebaud S, Bouzerar R and Bouzerar G 2017 *J. Phys. Chem. C* **121** 12577
[14] Lee C, Hong J, Lee W R, Kim D Y and Shim J H 2014 *Journal of Solid State Chemistry* **211** 113
[15] Wang K, Huang B, Tian M, Ceballos F, Lin M W, Mahjouri-Samani M, Boulesbaa A, Puretzky A A, Rouleau C M and Yoon M 2016 *ACS Nano* **10** 6612
[16] Jin C, Kim J, Utama M I B, Regan E C, Kleemann H, Cai H, Shen Y, Shinner M J, Sengupta A and Watanabe K 2018 *Science* **360** 893
[17] Li S, Zang W, Liu X, Pennycook S J, Kou Z, Yang C, Guan C and Wang J 2019 *Chemical Engineering Journal* **359** 1419
[18] Ceballos F, Bellus M Z, Chiu H Y and Zhao H 2014 *ACS Nano* **8** 12717
[19] Debbichi L, Eriksson O and Leb'egue S 2014 *Phys. Rev. B* **89** 205311
[20] Wang F Q, Liu J, Li X, Wang Q and Kawazoe Y 2017 *Appl. Phys. Lett.* **111** 192102
[21] Gao Y, Zhou Y and Hu M 2018 *J. Mater. Chem. A* **6** 18533
[22] Gao Y, Zhou Y, Zhang X and Hu M 2018 *J. Mater. Chem. C* **122** 9220
[23] Gao Y, Zhang X, Zhou Y and Hu M 2017 *J. Mater. Chem. C* **5** 10578
[24] Terrones H and Terrones M 2014 *Journal of Materials Research* **29** 373
[25] Duan X, Wang C, Shaw J C, Cheng R, Chen Y, Li H, Wu X, Tang Y, Zhang Q and Pan A 2014 *Nat. Nanotechnol.* **9** 1024
[26] Kresse G and Furthmüller J 1996 *Phys. Rev. B* **54** 11169
[27] Perdew J P, Burke K and Ernzerhof M 1996 *Phys. Rev. Lett.* **77** 3865
[28] Monkhorst H J and Pack J D 1976 *Phys. Rev. B* **13** 5188
[29] Zhang Y and Yang W 1998 *Phys. Rev. Lett.* **80** 890
[30] Mabiala-Poaty H, Douma D, M'Passi-Mabiala B and Mapasha R E 2018 *Journal of Physics and Chemistry of Solids* **120** 211
[31] Li W, Carrete J, Katcho N A and Mingo N 2014 *Computer Physics Communications* **185** 1747
[32] Li W, Mingo N, Lindsay L, Broido D A, Stewart D A and Katcho N A 2012 *Phys. Rev. B* **85** 195436
[33] Togo A, Oba F and Tanaka I 2008 *Phys. Rev. B* **78** 134106
[34] Feng T and Ruan X 2016 *Phys. Rev. B* **93** 045202
[35] Guo S D and Liu J T 2017 *Phys. Chem. Chem. Phys.* **19** 31982
[36] Qin D, Yan P, Ding G, Ge X, Song H and Gao G 2018 *Scientific Reports* **8** 1
[37] Rashid Z, Nissimagoudar A S and Li W 2019 *Phys. Chem. Chem. Phys.* **21** 5679
[38] Liu P F, Bo T, Liu Z, Eriksson O, Wang F, Zhao J and Wang B T 2018 *J. Mater. Chem. C* **6** 12689
[39] Molina-Sanchez A and Wirtz L 2011 *Phys. Rev. B* **84** 155413
[40] Huang L F, Gong P L and Zeng Z 2014 *Phys. Rev. B* **90** 045409
[41] Togo A and Tanaka I 2015 *Scripta Materialia* **108** 1
[42] Gu X and Yang R 2014 *Appl. Phys. Lett.* **105** 131903
[43] Yuan K, Zhang X, Li L and Tang D 2019 *Phys. Chem. Chem. Phys.* **21** 468
[44] Peng B, Zhang H, Shao H, Xu Y, Zhang X and Zhu H 2016 *RSC Adv.* **6** 5767
[45] Morelli D and Heremans J 2002 *Appl. Phys. Lett.* **81** 5126
[46] Peng C, Qin G, Zhang L, Zhang G, Wang C, Yan Y, Wang Y and Hu M 2018 *J. Phys. D: Appl. Phys.* **51** 315303
[47] Gu X, Li B and Yang R 2016 *J. Appl. Phys.* **119** 085106
[48] Lee S, Esfarjani K, Mendoza J, Dresselhaus M S and Chen G 2014 *Phys. Rev. B* **89** 085206
[49] Qin G and Hu M 2018 *npj Computational Materials* **4** 1
[50] Lee S, Esfarjani K, Luo T, Zhou J, Tian Z and Chen G 2014 *Nat. Commun.* **5** 1
[51] Guo R, Jho Y D and Minnich A J 2018 *Nanoscale* **10** 14432
[52] Peimyoo N, Shang J, Yang W, Wang Y, Cong C and Yu T 2015 *Nano Research* **8** 1210
[53] Jiang P, Qian X, Gu X and Yang R 2017 *Adv. Mater.* **29** 1701068
[54] Mobaraki A, Kandemir A, Yapicioglu H, Gülseren O and Sevik C 2018 *Computational Materials Science* **144** 92
[55] Gu X, Wei Y, Yin X, Li B and Yang R 2018 *Rev. Mod. Phys.* **90** 041002
[56] Gu X and Yang R 2015 *J. Appl. Phys.* **117** 025102
[57] Minnich A J, Johnson J A, Schmidt A J, Esfarjani K, Dresselhaus M S, Nelson K A and Chen G 2011 *Phys. Rev. Lett.* **107** 095901

[58] Liu P F, Bo T, Xu J, Yin W, Zhang J, Wang F, Eriksson O and Wang B T 2018 *Phys. Rev. B* **98** 235426
[59] Gao Y, Jing Y, Liu J, Li X and Meng Q 2017 *Applied Thermal Engineering* **113** 1419
[60] Togo A, Chaput L and Tanaka I 2015 *Phys. Rev. B* **91** 094306
[61] Lindsay L and Broido D 2008 *J. Phys.: Condens. Matter* **20** 165209
[62] Slack G A 1979 *Solid State Physics* **34** 1
[63] Shao H, Tan X, Hu T, Liu G Q, Jiang J and Jiang H 2015 *Europhys. Lett.* **109** 47004
[64] Ding Y and Xiao B 2015 *Rsc Advances* **5** 18391
[65] Mounet N and Marzari N 2005 *Phys. Rev. B* **71** 205214
[66] Morelli D, Jovovic V and Heremans J 2008 *Phys. Rev. Lett.* **101** 035901
[67] Yang S S, Hou Y and Zhu L L 2019 *Chin. Phys. B* **28** 086501
[68] Cai Y, Pei Q X, Zhang G and Zhang Y W 2016 *J. Appl. Phys.* **119** 065102
[69] Du A, Sanvito S, Li Z, Wang D, Jiao Y, Liao T, Sun Q, Ng Y H, Zhu Z and Amal R 2012 *J. Am. Chem. Soc.* **134** 4393